



# Controllable synthesis of Cu<sub>2</sub>O decorated WO<sub>3</sub> nanosheets with dominant (0 0 1) facets for photocatalytic CO<sub>2</sub> reduction under visible-light irradiation

Weina Shi<sup>a,\*</sup>, Xiaowei Guo<sup>a</sup>, Chengxing Cui<sup>b</sup>, Kai Jiang<sup>c</sup>, Zhongjun Li<sup>d</sup>, Lingbo Qu<sup>d</sup>,  
Ji-Chao Wang<sup>b,c,\*\*</sup>

<sup>a</sup> College of Chemistry and Chemical Engineering, Xinxiang University, Jinsui Avenue 191, Xinxiang, 453000, China

<sup>b</sup> Postdoctoral Research Base, School of Chemistry and Chemical Engineering, Henan Institute of Science and Technology, Eastern Hualan Avenue, Xinxiang, 453000, China

<sup>c</sup> Post-doctoral Station of Environmental Science and Engineering, Henan Normal University, Eastern Jianshe Road 46, Xinxiang, 453000, China

<sup>d</sup> College of Chemistry and Molecular Engineering, Zhengzhou University, Science Avenue 100, Zhengzhou, 450000, China

## ARTICLE INFO

### Keywords:

CO<sub>2</sub> reduction  
Hexagonal WO<sub>3</sub>  
Nanosheet  
Z-Scheme  
Cu<sub>2</sub>O  
Photocatalysis

## ABSTRACT

Systematical design and controllable assembly of nanostructured photocatalysts have received much attention in the field of CO<sub>2</sub> reduction. The Cu<sub>2</sub>O decorated hexagonal WO<sub>3</sub> nanosheets with and without dominant (0 0 1) facets (Cu<sub>2</sub>O/WO<sub>3</sub>-001 and Cu<sub>2</sub>O/WO<sub>3</sub>) were synthesized vertically on the surface of fluorine-doped stannic oxide (FTO) substrate and their photocatalytic performance for CO<sub>2</sub> reduction were evaluated in the presence of H<sub>2</sub>O vapour under visible light irradiation ( $\lambda > 400$  nm). The Cu<sub>2</sub>O/WO<sub>3</sub>-001 catalyst exhibited higher photocatalytic activity than those of Cu<sub>2</sub>O, WO<sub>3</sub>-001 and Cu<sub>2</sub>O/WO<sub>3</sub>. The maximal product yields of CO, O<sub>2</sub> and H<sub>2</sub> for Cu<sub>2</sub>O/WO<sub>3</sub>-001 after 24 h illumination reached 11.7, 5.7 and 0.7  $\mu$ mol, respectively, and good cycling ability was discovered after 4 cycles. The (0 0 1) facet of hexagonal phase WO<sub>3</sub> nanosheet was in favor of the H<sub>2</sub>O oxidation in the CO<sub>2</sub> reduction process. Additionally, the Z-scheme charge transfer mode of Cu<sub>2</sub>O/WO<sub>3</sub> heterojunction could promote photoinduced charge separation and enhance redox ability of the separated electrons and holes, leading to excellent photocatalytic CO<sub>2</sub> reduction performance. The study may provide some insights into the coherent design of specific nanosheet photocatalysts with Z-scheme charge transfer for CO<sub>2</sub> reduction.

## 1. Introduction

Photocatalytic reduction of CO<sub>2</sub> to produce valuable chemicals using solar energy has recently received considerable interests due to its great potential for reducing atmospheric CO<sub>2</sub> and supplying renewable fuels [1–3]. Photocatalytic CO<sub>2</sub> reduction requires an efficient catalyst that possesses excellent photo-absorption property in the visible light region and efficient extraction ability of the photogenerated electron-hole pairs to reactive sites [4]. However, the efficiency of photocatalytic CO<sub>2</sub> reduction over a single photocatalyst is very low and far from practical application, probably due to the shortages of its inherent physicochemical properties [5]. On going attempts for the construction of an efficient photocatalyst include nanostructuralization [6,7], tailoring of crystal phases [8], construction of heterojunctions [9,10], band-structure engineering [3,11] and so on, and significant progresses have been achieved to date.

Controlled assembly of nanostructured semiconductors offers a promising avenue for developing highly efficient photocatalysts for CO<sub>2</sub> reduction. Particularly, semiconductors with two-dimensional nanosheet structures could lead to short carrier diffusion length and efficient charge separation and migration [6,7], and many photons could be absorbed by the nanosheet in a remarkably short time due to its large surface area, which are favorable for enhancing the photocatalytic activity of multi-electron reaction [12]. It also has been verified that the size-quantization effects in nanosheets could change the band gap as well as the redox power of the semiconductor as compared with bulk catalysts, and thus modify the catalytic activity and selectivity of surface reaction, especially multi-electron reaction such as CO<sub>2</sub> reduction [13]. Furthermore, the construction of heterojunctions, especially typical all-solid-state Z-scheme systems, could promote photoinduced charge separation and enhance redox capacity of photoinduced electrons and holes, and thus improve the photocatalytic activity for CO<sub>2</sub>

\* Corresponding author at: College of Chemistry and Chemical Engineering, Xinxiang University, Jinsui Avenue 191, Xinxiang, 453000, China.

\*\* Corresponding author at: Postdoctoral Research Base, School of Chemistry and Chemical Engineering, Henan Institute of Science and Technology, Eastern Hualan Avenue, Xinxiang, 453000, China.

E-mail addresses: [shiweina516@163.com](mailto:shiweina516@163.com) (W. Shi), [wangjichao@hist.edu.cn](mailto:wangjichao@hist.edu.cn) (J.-C. Wang).

<https://doi.org/10.1016/j.apcatb.2018.09.076>

Received 26 June 2018; Received in revised form 11 September 2018; Accepted 23 September 2018

Available online 26 September 2018

0926-3373/ © 2018 Elsevier B.V. All rights reserved.

reduction [10,14,15]. Therefore, it is a practical way to explore effective photocatalysts by the construction of nanosheet-structured semiconductors and Z-scheme heterojunction systems with well-organized alignments.

WO<sub>3</sub> has attracted a great deal of interests in photocatalysis due to the medium band gap ( $E_g = 2.4 \sim 2.8$  eV), high oxidizing power of the valence band holes and good stability in acidic and oxidative conditions [16]. In particular, WO<sub>3</sub> nanosheets could be more effective in promoting charge separation and thus resulting in enhanced photocatalytic activity [17,18]. Chen et al. [11] reported that monoclinic WO<sub>3</sub> nanosheet exhibited better photocatalytic activity for CO<sub>2</sub> reduction than that of commercial WO<sub>3</sub> powder. Monoclinic and hexagonal WO<sub>3</sub> are the most attractive candidates among the various crystal phases. The monoclinic phase is the most stable phase, while the hexagonal phase possesses open-tunnel structure and rich intercalation chemistry [19]. Meanwhile, different crystalline structures of WO<sub>3</sub> could result in dissimilar electronic properties, and thus cause differences in photocatalytic activity for CO<sub>2</sub> reduction [20,21]. For example, Ohno et al. [22] showed that the monoclinic WO<sub>3</sub>/g-C<sub>3</sub>N<sub>4</sub> with Z-scheme exhibited good photocatalytic activity due to the facilitated transfer of electrons from CO<sub>2</sub> to CH<sub>3</sub>OH. Ying et al. [23] has proved that the (0 0 2) facets of monoclinic WO<sub>3</sub> could play a positive effect on the photocatalytic activity for CO<sub>2</sub> reduction. Furthermore, it is believed that the (0 0 1) facets of hexagonal WO<sub>3</sub> with suitable channels could be filled with H<sub>2</sub>O molecules, and act as fantastic chains for facilitating the electron transfer [4], which is theoretically favorable for photocatalytic reduction of CO<sub>2</sub> with H<sub>2</sub>O vapour [3]. However, the flat-band potential of electrons in the conduction band of hexagonal WO<sub>3</sub> is lower than that required for CO<sub>2</sub> reduction, resulting in the inability to reduce CO<sub>2</sub> solely by hexagonal WO<sub>3</sub> [18]. Hence, single hexagonal WO<sub>3</sub> photocatalyst has rarely been reported for CO<sub>2</sub> reduction. To solve these concerns, heterogeneous photocatalysts could be developed to further modify the redox capacity and photoinduced charge separation of the hexagonal WO<sub>3</sub>-based composites. Cu<sub>2</sub>O, a p-type semiconductor with a band gap of about 2.1 eV, is an attractive photocatalyst for CO<sub>2</sub> reduction [24–26], due to its intensive visible-light absorption ability and appropriate conduction band position (about -1.1 V vs. NHE). [11,20] Therefore, an effective way to address these issues may be provided by constructing a Cu<sub>2</sub>O/WO<sub>3</sub> Z-scheme system for photocatalytic CO<sub>2</sub> reduction.

To the best of our knowledge, few studies have been done over hexagonal WO<sub>3</sub>-based catalysts for CO<sub>2</sub> reduction. Herein, in this research, hexagonal WO<sub>3</sub> nanosheets with and without dominant (0 0 1) facets (WO<sub>3</sub>-001 and WO<sub>3</sub>) were synthesized by the seed-mediated hydrothermal methods, and Cu<sub>2</sub>O was electrodeposited onto the WO<sub>3</sub> nanosheets to fabricate Cu<sub>2</sub>O/WO<sub>3</sub>-001 and Cu<sub>2</sub>O/WO<sub>3</sub> composite photocatalysts. Photocatalytic activities for CO<sub>2</sub> reduction with H<sub>2</sub>O vapour were investigated, and the charge transfer mechanism for photocatalytic CO<sub>2</sub> reduction was further proposed for the WO<sub>3</sub>-based catalysts.

## 2. Experimental section

### 2.1. Synthesis of hexagonal WO<sub>3</sub> nanosheets with and without dominant (0 0 1) facets

All chemicals used in the experiments were of analytical grade and used without further purification. Hexagonal WO<sub>3</sub> nanosheets with and without dominant (0 0 1) facets were both synthesized on the fluorine-doped tin oxide (FTO) glass substrates through seed-mediated hydrothermal methods. [27] A H<sub>2</sub>WO<sub>4</sub> solution for the seed layer and hydrothermal growth was prepared by dissolving 1.25 g of H<sub>2</sub>WO<sub>4</sub> into 30 wt% H<sub>2</sub>O<sub>2</sub> and heated at 95 °C for 2 h. Before the hydrothermal growth, a seed layer was deposited onto the FTO substrate by spinning the above H<sub>2</sub>WO<sub>4</sub> solution with subsequent annealing treatment at 500 °C in air for 2 h. In a typical synthesis of WO<sub>3</sub> nanosheets with dominant (0

0 1) facets, a seeded FTO substrate was put into a Teflon-lined stainless steel autoclave with vertically orientation. Then, a mixed solution containing 3.0 mL of H<sub>2</sub>WO<sub>4</sub> solution, 0.5 mL of HCl (6 M) and 12.5 mL of acetonitrile was added into the reactor for the hydrothermal reaction at 180 °C for 6 h. Afterward, the as-prepared sample was rinsed with deionized water, dried in air, and annealed at 500 °C for 0.5 h. The obtained sample was denoted as WO<sub>3</sub>-001. Hexagonal phase WO<sub>3</sub> nanosheets without dominant (0 0 1) facets were prepared using the similar procedure, except that the hydrothermal solution was prepared by mixing 3.0 mL of H<sub>2</sub>WO<sub>4</sub> solution, 1.5 mL of HCl (5 M) and 10.5 mL of acetonitrile together, and the obtained sample was denoted as WO<sub>3</sub>.

### 2.2. Synthesis of Cu<sub>2</sub>O/WO<sub>3</sub> samples

Cu<sub>2</sub>O was electrodeposited on the surface of WO<sub>3</sub>-001 and WO<sub>3</sub> nanosheets using a modified method. [28] Typically, the deposition was conducted at -0.4 V in 0.5 M Cu(OAc)<sub>2</sub> aqueous solution using a standard three-electrode system, which was composed of WO<sub>3</sub>-001 and WO<sub>3</sub> nanosheet working electrodes, a platinum counter electrode, and a Ag/AgCl reference electrode. After deposition, the obtained samples were rinsed with deionized water and dried in air. The as-prepared materials were denoted as Cu<sub>2</sub>O/WO<sub>3</sub> and Cu<sub>2</sub>O/WO<sub>3</sub>-001. The control samples Cu<sub>2</sub>O/WO<sub>3</sub>-001-m and Cu<sub>2</sub>O/r-WO<sub>3</sub>-001 were also synthesized and the detailed process was described in the supplementary material.

### 2.3. Catalysts characterization

The crystal phases of the samples were recorded with X-ray diffractometer (PANalytical X'pert PRO, Netherlands). The BET surface areas were determined by N<sub>2</sub> adsorption-desorption isotherm measurements at 77 K (Autosorb-iQ, USA), and low-pressure CO<sub>2</sub> adsorption isotherms were conducted at 273 K for both WO<sub>3</sub> and WO<sub>3</sub>-001. The pore-size analysis of the prepared sample was based on a nonlocal density functional theory (NLDFT) model. A scanning electron microscope (SEM, Nova NanoSEM 450, FEI) was used to characterize the morphologies of the obtained samples. Transmission electron microscopy (TEM) images were obtained on a Tecnai G<sup>2</sup> F20 S-TWIN electron microscope. Furthermore, high-resolution transmission electron microscopy (HRTEM) and energy dispersive X-Ray spectroscopy (EDX) were employed. X-ray photoelectron spectroscopy (XPS) measurements were carried out at room temperature on a Thermo escalab 250Xi X-ray Photoelectron Spectrometer. UV–vis absorption spectra were performed on a Cary 5000 scan UV–vis spectrometer.

### 2.4. Photocatalytic performance tests

The photocatalytic experiment for the reduction of CO<sub>2</sub> with H<sub>2</sub>O vapour was carried out in a stainless steel cylindrical vessel with a quartz window on top of the reactor. A 300 W Xenon arc lamp (PLS-HXF 300, Beijing China Education Au-light Co. Ltd., China) with a UV cutoff filter ( $\lambda > 400$  nm) was utilized as the light source. The catalyst (about 85 mg was placed on a glass sheet (1.8 × 2.0 cm<sup>2</sup>) inside the reactor. Prior to light irradiation, the reaction setup was vacuum treated, and then purged with high purity CO<sub>2</sub> gas (99.995%) for several times. The compressed high purity CO<sub>2</sub> gas was passed through a water bubbler to generate a mixture of CO<sub>2</sub> and H<sub>2</sub>O vapour. After illumination, the gaseous products were quantifiably identified using an off-line GC-7890II gas chromatograph (Techcomp Corp., China) equipped with both a flame ionization detector (FID) and a thermal conductivity detector (TCD). The equipped columns were TDX-01 and Porapak-Q, respectively. Then, other hydrocarbon products were analyzed by GC-MS (Agilent 7890A-5975C) equipped with a DB-FFAP capillary column. The isotope-labeled experiments were performed using <sup>13</sup>CO<sub>2</sub> instead of <sup>12</sup>CO<sub>2</sub>, and the products were analyzed using GC-MS. In order to evaluate the stability, the composites were refreshed by the electrochemical treatment before washing and drying,

and their photocatalytic performances were reassessed. Photoelectrochemical test was conducted in a conventional three-electrode system using a CHI 660E electrochemical workstation (Chenhua, Shanghai, China). Photocurrents of the photocatalysts were measured at 0.0 V (vs. Ag/AgCl) in 0.5 M Na<sub>2</sub>SO<sub>4</sub> aqueous solution under light illumination, and dissolved oxygen was removed by purging with high purity nitrogen gas before the measurements. Apparent quantum efficiency (AQY) of the as-prepared samples at 420 nm was defined by the following equation because of a 2-hole process for the production of CO as a main product from CO<sub>2</sub> reduction: [22]

$$AQY(\%) = \frac{2 \times N_{CO}}{\text{Number of incident photons}} \times 100\% \quad (1)$$

\*  $N_{CO}$  represented the number of evolved CO molecules.

In the photocatalytic O<sub>2</sub> evolution experiment, 80 mg of photocatalyst was suspended in 100 mL of water with and without adding KBrO<sub>3</sub> electron scavenger. The reactant solution was thoroughly degassed under flowing high-purity N<sub>2</sub> for 90 min in prior. The reaction solution was magnetically stirred and the temperature of the reaction system was maintained below 4 °C during the entire experiment. The evolved O<sub>2</sub> was analyzed through a gas chromatograph (Agilent GC-6890, 5 A molecular sieve column) equipped with a thermal conductivity detector using high-purity Ar (99.999 vol%) as the carrier gas.

### 3. Results and discussion

#### 3.1. Composition, structure and morphology

XRD patterns of the as-prepared materials were shown in Fig. 1. WO<sub>3</sub> sample exhibited pronounced diffraction peaks at 13.9°, 22.7°, 24.3°, 26.8° and 28.2°, corresponding to (1 0 0), (0 0 1), (1 1 0), (1 0 1) and (2 0 0) facets of hexagonal phase WO<sub>3</sub> (JCPDS No. 33-1387). The peak intensity of (0 0 1) facets for WO<sub>3</sub>-001 nanosheet was obviously enhanced, which was caused by exposing the specific facets. By measuring the respective peak areas of the (1 0 0), (0 0 1) and (2 0 0) facets, the fraction of (0 0 1) facets from XRD patterns was estimated by the following equation (Eq. (1)). [27]

$$w_{(0\ 0\ 1)} = \Sigma A_{(0\ 0\ 1)} / [\Sigma A_{(1\ 0\ 0)} + \Sigma A_{(0\ 0\ 1)} + \Sigma A_{(2\ 0\ 0)}] \quad (2)$$

The calculated percentage of (0 0 1) facets for WO<sub>3</sub> and WO<sub>3</sub>-001 are about 25% and 68%, respectively. Additionally, cubic Cu<sub>2</sub>O (JCPDS No. 01-078-2076) was successfully electrodeposited onto the WO<sub>3</sub>-001 and WO<sub>3</sub> samples, respectively. The obtained Cu<sub>2</sub>O/WO<sub>3</sub>-001 and Cu<sub>2</sub>O/WO<sub>3</sub> composites exhibited characteristic diffraction peaks of both WO<sub>3</sub> and Cu<sub>2</sub>O, and no impurity peaks were detected, indicating that the deposition of Cu<sub>2</sub>O didn't alter the crystalline phase of WO<sub>3</sub>.

X-ray photoelectron spectroscopy (XPS) measurements were carried

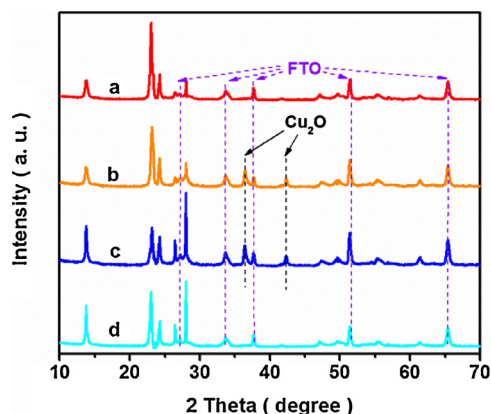


Fig. 1. XRD patterns of WO<sub>3</sub>-001 (a), Cu<sub>2</sub>O/WO<sub>3</sub>-001 (b), Cu<sub>2</sub>O/WO<sub>3</sub> (c) and WO<sub>3</sub> (d).

out to elucidate the surface composition and chemical states of the samples. The survey XPS spectra (Fig. S1) indicated that the composites were composed of W, Cu and O elements. The high resolution XPS spectra of W 4f and Cu 2p in Fig. 2 were deconvoluted by the Gaussian-Lorentzian method. As shown in Fig. 2a, two distinct peaks centered at binding energies of 35.5 and 37.7 eV corresponded to W<sup>6+</sup> oxidation state of WO<sub>3</sub>-001, while the relatively weak peaks at 34.5 and 36.5 eV were attributed to W<sup>5+</sup> oxidation state, [29,30] which was necessary to maintain its hexagonal phase structure [31]. Besides, Cu<sub>2</sub>O/WO<sub>3</sub>-001 exhibited higher W<sup>5+</sup>/W<sup>6+</sup> ratio than that of WO<sub>3</sub>-001 from Fig. 2a, which indicated that W<sup>6+</sup> species were partially reduced during the electrodeposition of Cu<sub>2</sub>O. As shown in the high resolution Cu 2p XPS spectra (Fig. 2b), the Cu<sub>2</sub>O/WO<sub>3</sub>-001 sample exhibited two characteristic peaks centered at 932.6 and 952.3 eV, corresponding to Cu<sup>+</sup> 2p<sub>3/2</sub> and 2p<sub>1/2</sub>, respectively. Two weak peaks were also observed at binding energies of 933.5 eV for Cu<sup>2+</sup> 2p<sub>3/2</sub> and 953.6 eV for Cu<sup>2+</sup> 2p<sub>1/2</sub> [32], and the other two tiny shakeup satellite peaks centered at 940.4 and 960.7 eV further confirmed the coexistence of a trace amount of CuO having a d<sup>9</sup> configuration in the ground state, which may be due to surface oxidation of Cu<sub>2</sub>O in air. [33] Furthermore, the Cu 2p and W 4f peaks of Cu<sub>2</sub>O/WO<sub>3</sub>-001 were positively shifted in comparison with those of pure Cu<sub>2</sub>O and WO<sub>3</sub>-001, which can be attributed to the intense interaction between WO<sub>3</sub>-001 and Cu<sub>2</sub>O, implying that the heterojunctions have been formed in the as-synthesized composites.

The morphologies and micro-structural information of the as-prepared samples were visualized by SEM and TEM measurements. Fig. 3 showed SEM and TEM images of the as-prepared samples. As can be seen, nanosheets were successfully grown on FTO substrates for WO<sub>3</sub> (Fig. 3a) and WO<sub>3</sub>-001 (Fig. 3b), and free spaces were clearly observed among the nanosheets, which were beneficial for full contact between catalysts and reactant gas. The TEM images of WO<sub>3</sub>-001 (Fig. 3c) revealed a typical nanosheet morphology, and the HRTEM image (inset of Fig. 3c) of WO<sub>3</sub>-001 showed lattice fringes with interplanar spacings of 0.634 and 0.366 nm, which were consistent with (1 0 0) and (1 1 0) facets of hexagonal phase WO<sub>3</sub>, respectively. As shown in Fig. S2a, the WO<sub>3</sub>-001 showed a maximal pore peak at 0.41 nm, which may be due to the pore structure on the (0 0 1) facets of hexagonal WO<sub>3</sub>. Additionally, the CO<sub>2</sub> adsorption isotherm of WO<sub>3</sub> exhibited a large uptake at low relative pressure (Fig. S2b), which indicated the presence of micro-sized tunnels in the structure of the hexagonal phase WO<sub>3</sub> nanosheet [34], and the CO<sub>2</sub> adsorption ability of WO<sub>3</sub>-001 was stronger than that of WO<sub>3</sub> sample. Based on hexagonal phase WO<sub>3</sub>, six tungsten oxide octahedral building blocks sharing their corners assemble into one six-membered ring with a diameter of 0.53 nm [35]. The analysis resulted in the plane of WO<sub>3</sub> nanosheet along with the [0 0 1] axis direction, which indicated that the (0 0 1) facet was exposed on the nanosheet surface. Furthermore, the Cu<sub>2</sub>O/WO<sub>3</sub> (Fig. 3d) and Cu<sub>2</sub>O/WO<sub>3</sub>-001 (Fig. 3e) exhibited similar nanosheet morphologies as compared with those of bare WO<sub>3</sub> and WO<sub>3</sub>-001. The pronounced diffraction fringe of the HRTEM image (inset of Fig. 3f) showed d-spacings of 0.246 and 0.213 nm, corresponding to the (1 1 1) and (2 0 0) facets of cubic Cu<sub>2</sub>O, respectively [36,37]. To further explore the detailed elemental distributions, energy-filtered W, Cu, and O maps of the Cu<sub>2</sub>O/WO<sub>3</sub>-001 sample were constructed and shown in Fig. S3. As can be seen, all the elements were homogeneously distributed, indicating that Cu<sub>2</sub>O was uniformly deposited on the surface of WO<sub>3</sub> nanosheet by the electroreduction method.

#### 3.2. Photocatalytic performance for CO<sub>2</sub> reduction

The photocatalytic CO<sub>2</sub> reduction activities of the catalysts were evaluated in the presence of H<sub>2</sub>O vapour under continuous visible-light irradiation ( $\lambda > 400$  nm) for 24 h. As shown in Fig. 4, no products were observed after illumination for 18 h over Cu<sub>2</sub>O, WO<sub>3</sub> and WO<sub>3</sub>-001 catalysts. However, the CO, O<sub>2</sub> and H<sub>2</sub> products were detected for the composite catalysts. To provide solid evidence to validate the origin



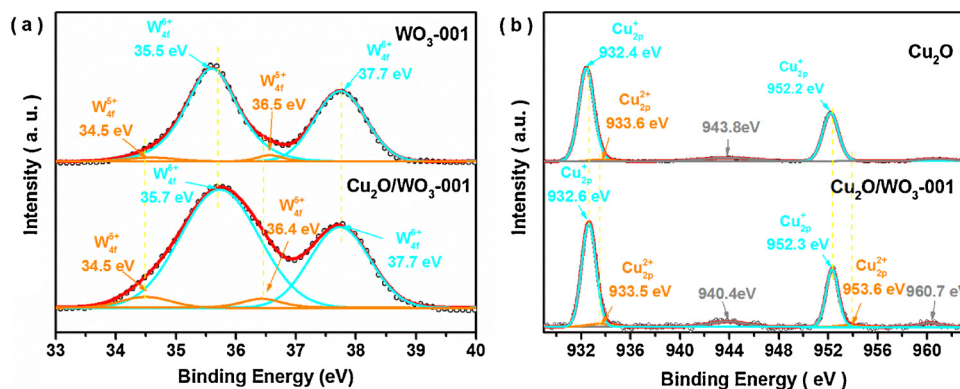


Fig. 2. W 4f (a) and Cu 2p (b) XPS spectra of Cu<sub>2</sub>O, WO<sub>3</sub>-001 and Cu<sub>2</sub>O/WO<sub>3</sub>-001.

of the generated CO, a <sup>13</sup>C labelled isotropic experiment was carried out by using <sup>13</sup>CO<sub>2</sub> to replace <sup>12</sup>CO<sub>2</sub>. The produced CO was analyzed by GC–MS, and the results were shown in Fig. S4. As can be seen, when <sup>13</sup>CO<sub>2</sub> was used as the reactant, <sup>13</sup>CO ( $m/z = 29$ ) was detected, which was significantly different from the detected <sup>12</sup>CO ( $m/z = 28$ ) when using <sup>12</sup>CO<sub>2</sub> as the reactant. For comparison, the photocatalytic performance of the mechanically dispersed Cu<sub>2</sub>O/WO<sub>3</sub>-001-m sample was investigated to corroborate the heterojunction effect, and the results showed that tiny amounts of potential products such as CO and O<sub>2</sub> were detected for the mechanically dispersed Cu<sub>2</sub>O/WO<sub>3</sub>-001-m sample, which indicated that the loosely contacted interfaces were insufficient for photocatalytic reduction of CO<sub>2</sub>. The results of this isotropic experiment validated that the composite catalysts indeed effectively accelerate photocatalytic transformation of CO<sub>2</sub> to CO. Besides, the XPS spectra of the photocatalysts after illumination were deconvoluted, and the peak area ratios of Cu<sup>2+</sup>/Cu<sup>+</sup> and W<sup>5+</sup>/W<sup>6+</sup> have been summarized in Table S1. The W<sup>5+</sup> content in composites distinctly decreased, compared with that in pure WO<sub>3</sub>-001. It indicated the possible formation of heterojunction between Cu<sub>2</sub>O and WO<sub>3</sub>-001 for the composite. Moreover, Cu<sub>2</sub>O/WO<sub>3</sub>-001 composite exhibited higher photocatalytic activity for CO<sub>2</sub> reduction than that of Cu<sub>2</sub>O/WO<sub>3</sub> catalyst and the W<sup>5+</sup> content kept a lower value than those in other catalysts, which implied that the dominant (0 0 1) facets in WO<sub>3</sub>-001 nanosheet could inhibit the

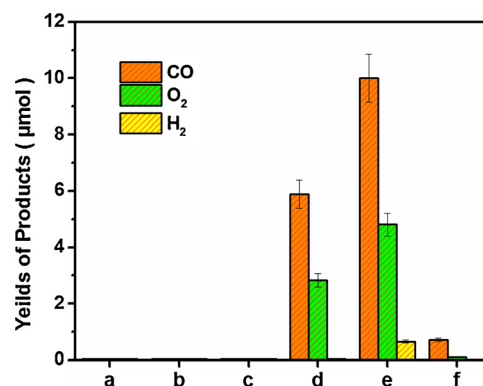


Fig. 4. Photocatalytic performance of CO<sub>2</sub> reduction over Cu<sub>2</sub>O (a), WO<sub>3</sub> (b), WO<sub>3</sub>-001 (c), Cu<sub>2</sub>O/WO<sub>3</sub> (d), Cu<sub>2</sub>O/WO<sub>3</sub>-001 (e) and Cu<sub>2</sub>O/WO<sub>3</sub>-001-m (f) samples under continuous visible-light irradiation ( $\lambda > 400$  nm) for 18 h.

reduction of W<sup>5+</sup> in composites. The phenomena may be attributed to the following factors. Firstly, for the Cu<sub>2</sub>O/WO<sub>3</sub>-001 sample, the six tungsten oxide (WO<sub>6</sub>) octahedral building blocks of hexagonal phase WO<sub>3</sub> shared their corners and assembled into one six-membered ring on (0 0 1) facets [34], and the interstitial spaces could readily

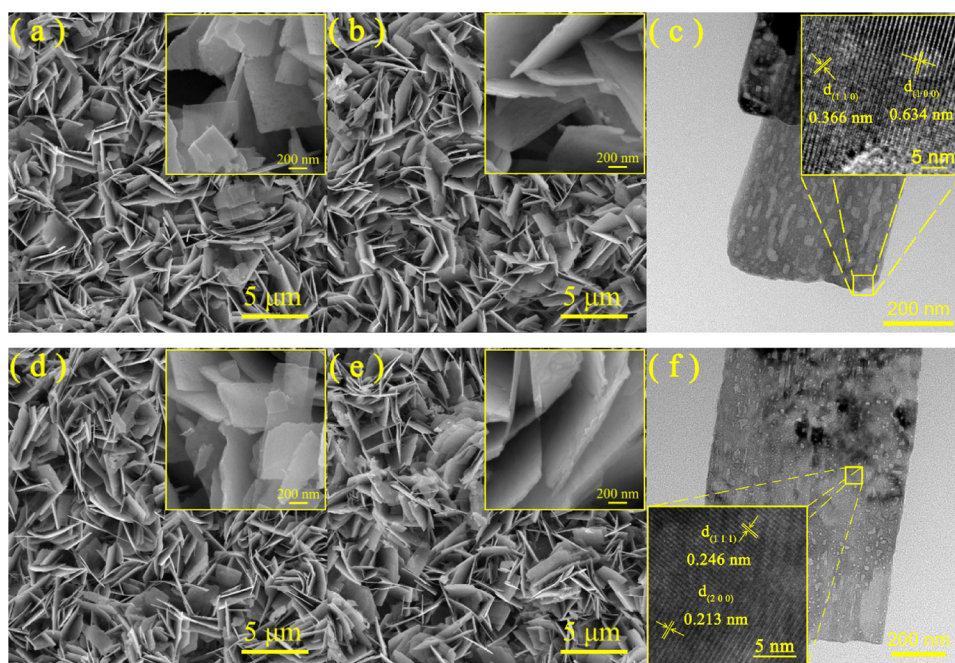


Fig. 3. SEM and TEM images of WO<sub>3</sub> (a), WO<sub>3</sub>-001 (b, c), Cu<sub>2</sub>O/WO<sub>3</sub> (d) and Cu<sub>2</sub>O/WO<sub>3</sub>-001 (e, f) samples.

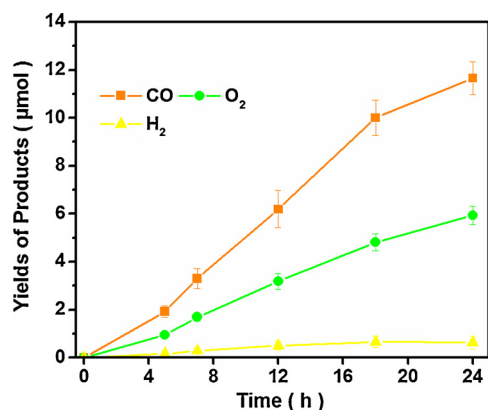


Fig. 5. Total yields of the products over the Cu<sub>2</sub>O/WO<sub>3</sub>-001 catalyst with different irradiation times.

accommodate guest molecules and ions (e.g. H<sub>2</sub>O and H<sup>+</sup>). [35] To investigate the influence of (0 0 1) facet on H<sub>2</sub>O oxidation, the photocatalytic activity for O<sub>2</sub> evolution was measured and shown in Fig. S5. Due to the weak reduction ability of photoinduced electrons, few O<sub>2</sub> and H<sub>2</sub> were produced in pure water for WO<sub>3</sub> and WO<sub>3</sub>-001. With the addition of KBrO<sub>3</sub>, as an electron scavenger, the photocatalytic O<sub>2</sub> yield of WO<sub>3</sub>-001 was distinctly higher than that of WO<sub>3</sub>. It indicated that the (0 0 1) facets enabled effective hole conduction throughout the micropore channels of WO<sub>3</sub>-001 [35]. Besides, the apparent quantum efficiencies (AQY) of the as-prepared composites at 420 nm were summarized in Table S2. The AQY of Cu<sub>2</sub>O/WO<sub>3</sub>-001 reached 0.503%, which was about twice that of Cu<sub>2</sub>O/WO<sub>3</sub>. Hence, the (0 0 1) facet of hexagonal phase WO<sub>3</sub> was in favor of the transfer between the photo-induced charges and the adsorbed water molecules, conducting to H<sub>2</sub>O oxidation in the CO<sub>2</sub> reduction process, and thus Cu<sub>2</sub>O/WO<sub>3</sub>-001 exhibited better photocatalytic activity for CO<sub>2</sub> reduction.

Fig. 5 showed the photocatalytic activity of the Cu<sub>2</sub>O/WO<sub>3</sub>-001 sample for CO<sub>2</sub> reduction. As can be seen, CO was detected as the major reduction product, and small amounts of H<sub>2</sub> and O<sub>2</sub> were also generated, which indicated that the photocatalytic reduction of CO<sub>2</sub> was thermodynamically favorable for the formation of CO through a two-electron reduction, due to the proton-assisted multi-electrons pathway of CO<sub>2</sub> reduction [38]. The total yields of CO, H<sub>2</sub> and O<sub>2</sub> enhanced with the prolongation of the irradiation time to 24 h, and finally reached 11.7, 5.7 and 0.7 μmol, respectively. However, a slight decrease of the production rates occurred throughout the whole process. The maximal production rates of CO and O<sub>2</sub> were found at 18 h to be 0.56 and 0.27 μmol·h<sup>-1</sup>, respectively (Fig. S6). The recession of the photocatalytic yield rates may be due to oxidation of the products or formation of intermediates covering the surface active sites of photocatalysts.

Recycling photostability of the Cu<sub>2</sub>O/WO<sub>3</sub>-001 catalyst was investigated, and the results were shown in Fig. 6. As can be seen, the yields of CO, H<sub>2</sub> and O<sub>2</sub> decreased slightly after four cycles in spite of the electrochemical regeneration. Typically, the yield of CO decreased to 10.1 μmol after the fourth cycle, about 86.3% of that of the first run. XPS analysis was further applied to investigate the stability of the catalyst. In the high resolution XPS spectra of Cu<sub>2</sub>O/WO<sub>3</sub>-001 catalyst after the fourth cycle (Fig. S7 and Table S3), the peak positions of Cu 2p and W 4f remained nearly unchanged as compared with those of the fresh catalyst. Unfortunately, an obvious raising of W<sup>5+</sup>/W<sup>6+</sup> ratio was observed after four cycles. For exploring the role of W<sup>5+</sup> for photocatalysis, a large amount of W<sup>5+</sup> was obtained for the controlled sample Cu<sub>2</sub>O/r-WO<sub>3</sub>-001 by an electro-reduction method. Based on the XPS measurement (Fig. S8), a mass of W<sup>5+</sup> existed in the Cu<sub>2</sub>O/r-WO<sub>3</sub>-001, and scarcely any products including CO, CH<sub>4</sub>, H<sub>2</sub> and O<sub>2</sub> were found, based on the GC–MS results. Hence, the excess W<sup>5+</sup> in WO<sub>3</sub> component

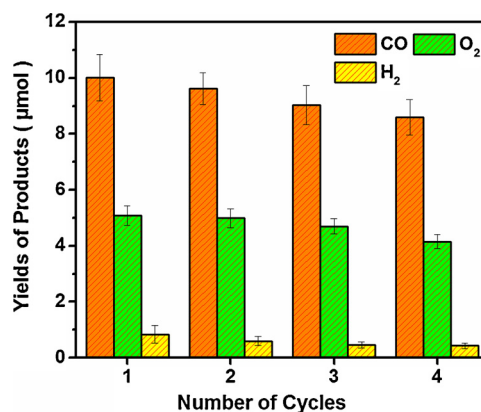


Fig. 6. Recyclability test of the Cu<sub>2</sub>O/WO<sub>3</sub>-001 catalyst under visible-light illumination for 18 h.

led to the decline of photocatalytic performance.

The mechanism of photocatalytic CO<sub>2</sub> reduction was related to the redox abilities of photo-induced electrons and holes, which were influenced by the energy positions of conduction and valence band edges. We determined the electronic band structures of the photocatalysts by UPS and DRS spectra. As shown in Fig. S9, the calculated  $E_g$  values for WO<sub>3</sub>, WO<sub>3</sub>-001 and Cu<sub>2</sub>O were 2.75, 2.86 and 2.05 eV, respectively. Fig. 7 showed the UPS spectra of Cu<sub>2</sub>O, WO<sub>3</sub> and WO<sub>3</sub>-001 samples measured at the same voltage of -8.0 V. According to the linear intersection method, [38] the valence band edge energy ( $E_{VB}$ ) of Cu<sub>2</sub>O was estimated to be -5.56 eV (vs. vacuum), and the conduction band edge energy ( $E_{CB}$ ) was calculated to be -3.57 eV (vs. vacuum) from the  $E_g$  and  $E_{VB}$  values. The corresponding  $E_{VB}$  and  $E_{CB}$  values of Cu<sub>2</sub>O were 0.91 and -1.12 eV (vs. NHE), respectively, based on the connection between the normal electrode potential ( $E^0$ ) and the vacuum energy ( $E_{abs}$ ),  $E_{abs} = -E^0 - 4.44$  [33]. Similarly, the calculated values of  $E_{CB}$  and  $E_{VB}$  for WO<sub>3</sub>-001 were 0.02 and 2.88 eV (vs. NHE) and those of WO<sub>3</sub> were 0.15 and 2.90 eV (vs. NHE). These band energies agreed well with the previously reported values [39], and there were no distinct differences for the band energies between WO<sub>3</sub> and WO<sub>3</sub>-001. A staggered band alignment heterostructure was successfully formed, assuming that the possible band bending of the semiconductor is neglected.

Transient photocurrent responses were further recorded over several on-off irradiation cycles to demonstrate the separation of photo-generated charge carriers. As shown in Fig. S10, the photocurrents of the catalysts reproducibly increased under irradiation and quickly recovered in the dark. Besides, the photocurrent of the Cu<sub>2</sub>O/WO<sub>3</sub>-001 sample was about 5 and 15 times higher than those of pure WO<sub>3</sub>-001 and Cu<sub>2</sub>O, indicating the reduced recombination and efficient separation of electron-hole pairs in the composite.

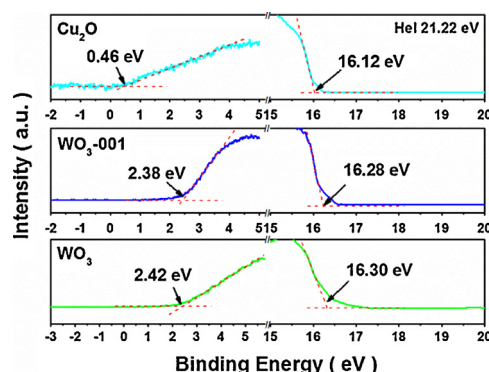


Fig. 7. UPS spectra of the as-prepared Cu<sub>2</sub>O, WO<sub>3</sub> and WO<sub>3</sub>-001 samples.

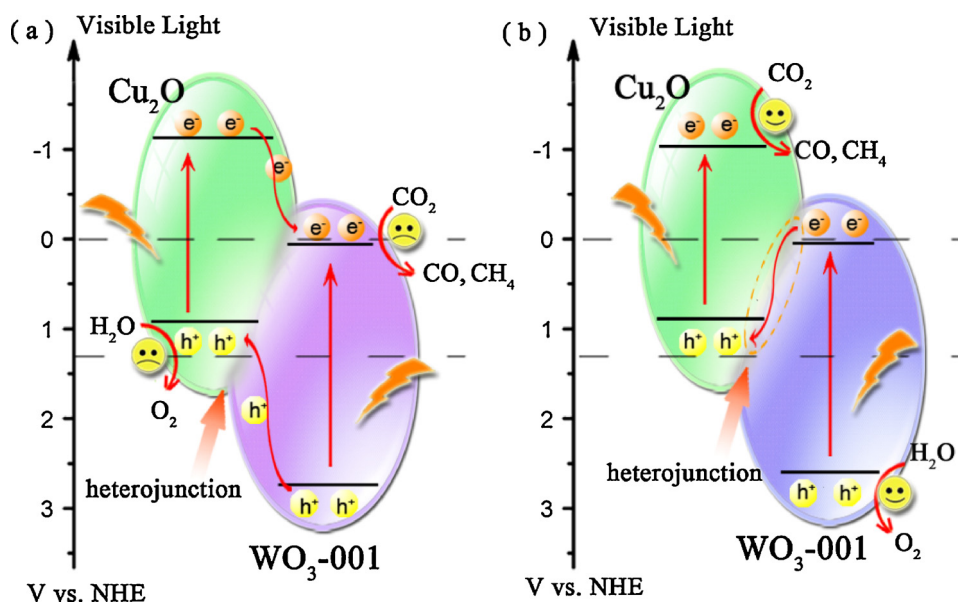


Fig. 8. Schematic illustration of the proposed charge transfer mechanisms: the common charge transfer mode (a) and Z-scheme charge transfer mode (b) for  $\text{Cu}_2\text{O}/\text{WO}_3$ -001.

### 3.3. Possible photocatalytic mechanism

On the basis of the experimental results and the band energy structure of the  $\text{Cu}_2\text{O}/\text{WO}_3$ -001 sample, the enhanced photocatalytic  $\text{CO}_2$  activity can be deduced as follows. The p-n junction could be formed at the interface of  $\text{WO}_3$ -001 and  $\text{Cu}_2\text{O}$ , resulting in the inner electrical field established in the direction from the n-type  $\text{WO}_3$  to the p-type  $\text{Cu}_2\text{O}$ . When exposing to the simulated light, the VB electrons of both  $\text{WO}_3$ -001 and  $\text{Cu}_2\text{O}$  could be excited. The possible separation process of the photoexcited electron-hole pairs at the interfacial phases can be schematically described in Fig. 8a and 8b. If the photoexcited charge carriers transferred adopting the common double charge transfer mode according to Fig. 8a, the accumulated electrons in the CB of  $\text{WO}_3$ -001 regrettably cannot realize the  $\text{CO}_2$  reduction to CO or  $\text{H}_2\text{O}$  reduction to  $\text{H}_2$ , which was due to that the calculated CB edge potential of  $\text{WO}_3$  (0.19 V vs. NHE) was more positive than the potential for  $\text{CO}_2$  reduction ( $\text{CO}/\text{CO}_2 = -0.11$  V vs. NHE) [3]. Simultaneously, the VB edge potential of  $\text{Cu}_2\text{O}$  (0.91 V vs. NHE) was more negative than that of  $\text{H}_2\text{O}$  oxidation ( $\text{O}_2/\text{H}_2\text{O} = 1.23$  V vs. NHE), and  $\text{O}_2$  production cannot be observed. Furthermore, the photo-induced electrons in the CB of  $\text{WO}_3$  could cause self-reduction of  $\text{W}^{6+}$  to  $\text{W}^{5+}$  in  $\text{WO}_3$  component. According to the promoted photocatalytic activity, the separation of photogenerated carriers was thought to be followed by the Z-scheme mechanism as shown in Fig. 8b. The photo-induced holes tend to remain in the VB of  $\text{WO}_3$ , and the electrons in the CB of  $\text{WO}_3$  were transferred to the CB of  $\text{Cu}_2\text{O}$ , which results in effective charge separation.  $\text{H}_2\text{O}$  oxidation can be achieved by the photo-induced holes in the VB of  $\text{WO}_3$ , and  $\text{CO}_2$  with  $\text{H}_2\text{O}$  vapour can be reduced by the accumulated electrons in the CB of  $\text{Cu}_2\text{O}$ . Photocatalytic reduction of  $\text{CO}_2$  into CO required two electrons, which was dynamically favored than the formation of other fuels such as  $\text{CH}_4$  and  $\text{CH}_3\text{OH}$ . Products such as CO,  $\text{H}_2$  and  $\text{O}_2$  can be detected for the photocatalytic  $\text{CO}_2$  reduction with  $\text{H}_2\text{O}$  vapor under visible-light illumination in the experiments. Based on the decline of  $\text{W}^{5+}/\text{W}^{6+}$  ratio in the  $\text{Cu}_2\text{O}/\text{WO}_3$ -001 composite as compared with those in the  $\text{Cu}_2\text{O}/\text{WO}_3$  and  $\text{WO}_3$ -001 samples (Table S1), the  $\text{W}^{5+}$  formation was inhibited in the  $\text{Cu}_2\text{O}/\text{WO}_3$ -001 composite. It indicated that the photogenerated electrons in  $\text{WO}_3$  component was effectively derived by the heterojunction. Consequently, the  $\text{Cu}_2\text{O}/\text{WO}_3$ -001 composite was a direct Z-scheme photocatalyst.

### 4. Conclusions

In summary, hexagonal-phase  $\text{WO}_3$  nanosheet with dominant (0 0 1) facets was synthesized by a solvothermal-calcination method, and  $\text{Cu}_2\text{O}$  was composite and the electrodeposition method. The  $\text{Cu}_2\text{O}/\text{WO}_3$ -001 composite nanosheets exhibited an excellent photocatalytic  $\text{CO}_2$  reduction performance under visible irradiation ( $\lambda > 400$  nm). The yields of CO,  $\text{O}_2$  and  $\text{H}_2$  using  $\text{Cu}_2\text{O}/\text{WO}_3$ -001 photocatalysts reached 11.7, 5.7 and 0.7  $\mu\text{mol}$ , respectively, after 24 h visible-light illumination and the photocatalyst showed good photocatalytic activity in the fourth cycling test. The enhanced photocatalytic activity was ascribed to the efficient separation of the photoinduced charges derived from the constructed heterojunction in the nanosheet composite. The (0 0 1) facet of hexagonal phase  $\text{WO}_3$  was in favor of the transfer between the photo-induced holes and the water molecules, conducting to  $\text{H}_2\text{O}$  oxidation in the  $\text{CO}_2$  reduction process. The indirect Z-scheme charge transfer mode of  $\text{Cu}_2\text{O}/\text{WO}_3$  was then demonstrated by measuring band structures and the potential mechanism of  $\text{CO}_2$  reduction is further proposed. The present research is expected to be useful in developing Z-scheme photocatalysts of  $\text{WO}_3$ -based nanosheet, and provides meaningful information for hopefully stimulating more insightful investigations of systematical design and controlled assembly of visible-light-driven photocatalysts.

### Acknowledgements

This work was supported by National Natural Science Foundation of China (No. 51802082 and No. 21671059), China Postdoctoral Science Foundation Funded Project (No. 2017M612391), Key Scientific Research Project of Henan Province (18A150027), Key Scientific and Technological Project of Henan Province (182102311084) and Henan Postdoctoral Science Foundation.

### Appendix A. Supplementary data

Supplementary material related to this article can be found, in the online version, at doi:<https://doi.org/10.1016/j.apcatb.2018.09.076>.

### References

- [1] S.C. Roy, O.K. Varghese, P. Maggie, C.A. Grimes, Toward solar fuels: photocatalytic



- conversion of carbon dioxide to hydrocarbons, *ACS Nano* 4 (2010) 1259–1278.
- [2] S.N. Habisreutinger, L. Schmidt-Mende, J.K. Stolarczyk, Photocatalytic reduction of CO<sub>2</sub> on TiO<sub>2</sub> and other semiconductors, *Angew. Chem. Int. Ed.* 52 (2013) 7372–7408.
  - [3] W. Tu, Y. Zhou, Z. Zou, Photocatalytic conversion of CO<sub>2</sub> into renewable hydrocarbon fuels: state-of-the-art accomplishment, challenges, and prospects, *Adv. Mater.* 26 (2014) 4607–4626.
  - [4] D. Chen, X. Zhang, A.F. Lee, Synthetic strategies to nanostructured photocatalysts for CO<sub>2</sub> reduction to solar fuels and chemicals, *J. Mater. Chem. A* 3 (2015) 14487–14516.
  - [5] R. Marschall, Semiconductor composites: strategies for enhancing charge carrier separation to improve photocatalytic activity, *Adv. Funct. Mater.* 24 (2014) 2421–2440.
  - [6] H. Li, Y. Shi, M.-H. Chiu, L.-J. Lin, Emerging energy applications of two-dimensional layered transition metal dichalcogenides, *Nano Energy* 18 (2015) 293–305.
  - [7] A.I. Hochbaum, P. Yang, Semiconductor nanowires for energy conversion, *Chem. Rev.* 110 (2010) 527–546.
  - [8] F. Fresno, R. Portela, S. Suárez, J.M. Coronado, Photocatalytic materials: recent achievements and near future trends, *J. Mater. Chem. A* 2 (2014) 2863–2884.
  - [9] H. Wang, L. Zhang, Z. Chen, J. Hu, S. Li, Z. Wang, J. Liu, X. Wang, Semiconductor heterojunction photocatalysts: design, construction, and photocatalytic performances, *Chem. Soc. Rev.* 43 (2014) 5234–5244.
  - [10] P. Zhou, J. Yu, M. Jaroniec, All-solid-state Z-scheme photocatalytic systems, *Adv. Mater.* 26 (2014) 4920–4935.
  - [11] X. Chen, Y. Zhou, Q. Liu, Z. Li, J. Liu, Z. Zou, Ultrathin, single-crystal WO<sub>3</sub> nanosheets by two-dimensional oriented attachment toward enhanced photocatalytic reduction of CO<sub>2</sub> into hydrocarbon fuels under visible light, *ACS Appl. Mater. Interface* 4 (2012) 3372–3377.
  - [12] S. Ida, T. Ishihara, Recent progress in two-dimensional oxide photocatalysts for water splitting, *J. Phys. Chem. Lett.* 5 (2014) 2533–2542.
  - [13] M. Cargnello, B.T. Diroll, Tailoring photocatalytic nanostructures for sustainable hydrogen production, *Nanoscale* 6 (2014) 97–105.
  - [14] L.J. Zhang, S. Li, B.K. Liu, D.J. Wang, T.F. Xie, Highly efficient CdS/WO<sub>3</sub> photocatalysts: Z-scheme photocatalytic mechanism for their enhanced photocatalytic H<sub>2</sub> evolution under visible light, *ACS Catal.* 4 (2014) 3724–3729.
  - [15] D.J. Martin, P.J. Reardon, S.J. Moniz, J. Tang, Visible light-driven pure water splitting by a nature-inspired organic semiconductor-based system, *J. Am. Chem. Soc.* 136 (2014) 12568–12571.
  - [16] J. Wang, C.-J. Liu, Preparation of 2D WO<sub>3</sub> nanomaterials with enhanced catalytic activities: current status and perspective, *ChemBioEng Rev.* 2 (2015) 335–350.
  - [17] J. Yan, T. Wang, G. Wu, W. Dai, N. Guan, L. Li, J. Gong, Tungsten oxide single crystal nanosheets for enhanced multichannel solar light harvesting, *Adv. Mater.* 27 (2015) 1580–1586.
  - [18] Y. Zheng, G. Chen, Y. Yu, Y. Hu, Y. Feng, J. Sun, Urea-assisted synthesis of ultra-thin hexagonal tungsten trioxide photocatalyst sheets, *J. Mater. Sci.* 50 (2015) 8111–8119.
  - [19] D.B. Hernandez-Uresti, D. Sánchez-Martínez, A. Martínez-dela Cruz, S. Sepúlveda-Guzmán, L.M. Torres-Martínez, Characterization and photocatalytic properties of hexagonal and monoclinic WO<sub>3</sub> prepared via microwave-assisted hydrothermal synthesis, *Ceram. Int.* 40 (2014) 4767–4775.
  - [20] S. Yao, X. Zhang, F. Qu, A. Umar, X. Wu, Hierarchical WO<sub>3</sub> nanostructures assembled by nanosheets and their applications in wastewater purification, *J. Alloys Compd.* 689 (2016) 570–574.
  - [21] M. Pan, H. Zhang, G. Gao, L. Liu, W. Chen, Facet-dependent catalytic activity of nanosheet-assembled bismuth oxyiodide microspheres in degradation of bisphenol A, *Environ. Sci. Technol.* 49 (2015) 6240–6248.
  - [22] T. Ohno, N. Murakami, T. Koyanagi, Y. Yang, Photocatalytic reduction of CO<sub>2</sub> over a hybrid photocatalyst composed of WO<sub>3</sub> and graphitic carbon nitride (g-C<sub>3</sub>N<sub>4</sub>) under visible light, *J. CO<sub>2</sub> Util.* 6 (2014) 17–25.
  - [23] Y.P. Xie, G. Liu, L. Yin, H.-M. Cheng, Crystal facet-dependent photocatalytic oxidation and reduction reactivity of monoclinic WO<sub>3</sub> for solar energy conversion, *J. Mater. Chem.* 22 (2012) 6746–6751.
  - [24] J. Albo, A. Sáez, J. Solla-Gullón, V. Montiel, A. Iribien, Production of methanol from CO<sub>2</sub> electroreduction at Cu<sub>2</sub>O and Cu<sub>2</sub>O/ZnO-based electrodes in aqueous solution, *Appl. Catal. B* 176–177 (2015) 709–717.
  - [25] S. Zhu, S. Liang, Y. Tong, X. An, J. Long, X. Fu, X. Wang, Photocatalytic reduction of CO<sub>2</sub> with H<sub>2</sub>O to CH<sub>4</sub> on Cu(I) supported TiO<sub>2</sub> nanosheets with defective {0 0 1} facets, *Phys. Chem. Chem. Phys.* 17 (2015) 9761–9770.
  - [26] D. Ren, Y. Deng, A.D. Handoko, C.S. Chen, S. Malkhandi, B.S. Yeo, Selective electrochemical reduction of carbon dioxide to ethylene and ethanol on copper(I) oxide catalysts, *ACS Catal.* 5 (2015) 2814–2821.
  - [27] J. Zhang, P. Zhang, T. Wang, J. Gong, Monoclinic WO<sub>3</sub> nanomultilayers with preferentially exposed (0 0 2) facets for photoelectrochemical water splitting, *Nano Energy* 11 (2015) 189–195.
  - [28] J. Zhang, H. Ma, Z. Liu, Highly efficient photocatalyst based on all oxides WO<sub>3</sub>/Cu<sub>2</sub>O heterojunction for photoelectrochemical water splitting, *Appl. Catal. B* 201 (2017) 84–91.
  - [29] J. Liu, S. Yu, W. Zhu, X. Yan, Oxygen vacancy-enhanced visible light-driven photocatalytic activity of TiO<sub>2</sub> sphere-W<sub>18</sub>O<sub>49</sub> nanowire bundle heterojunction, *Appl. Catal. A Gen.* 500 (2015) 30–39.
  - [30] C. Yue, X. Zhu, M. Rigutto, E. Hensen, Acid catalytic properties of reduced tungsten and niobium-tungsten oxides, *Appl. Catal. B* 163 (2015) 370–381.
  - [31] I.M. Szilágyi, B. Fórizs, O. Rosseler, Á. Szegedi, P. Németh, P. Király, G. Tátrányi, B. Vajna, K. Varga-Josepovits, K. László, A.L. Tóth, P. Baranyai, M. Leskelä, Photocatalysts: influence of structure and composition, *J. Catal.* 294 (2012) 119–127.
  - [32] K.Y. Lee, H. Hwang, D. Shin, W. Choi, Enhanced thermo power wave via nanowire bonding and grain boundary fusion in combustion of fuel/CuO-Cu<sub>2</sub>O-Cu hybrid composites, *J. Mater. Chem. A* 3 (2015) 5457–5466.
  - [33] J.C. Wang, L. Zhang, W.X. Fang, J. Ren, Y.Y. Li, H.C. Yao, J.S. Wang, Z.J. Li, Enhanced photoreduction CO<sub>2</sub> activity over direct Z-scheme α-Fe<sub>2</sub>O<sub>3</sub>/Cu<sub>2</sub>O heterostructures under visible light irradiation, *ACS Appl. Mater. Interfaces* 7 (2015) 8631–8639.
  - [34] W. Sun, M.T. Yeung, A.T. Lech, C.W. Lin, C. Lee, T. Li, X. Duan, J. Zhou, R.B. Kaner, High surface area tunnels in hexagonal WO<sub>3</sub>, *Nano Lett.* 15 (2015) 4834–4838.
  - [35] Z. Hen, Y. Peng, F. Liu, Z. Le, J. Zhu, G. Shen, D. Zhang, M. Wen, S. Xiao, C.P. Liu, Y. Lu, H. Li, Hierarchical nanostructured WO<sub>3</sub> with biomimetic proton channels and mixed ionic-electronic conductivity for electrochemical energy storage, *Nano Lett.* 15 (2015) 6802–6808.
  - [36] W. Shi, X. Zhang, S. Li, B. Zhang, M. Wang, Y. Shen, Carbon coated Cu<sub>2</sub>O nanowires for photoelectrochemical water splitting with enhanced activity, *Appl. Surf. Sci.* 358 (2015) 404–411.
  - [37] S.-C. Wu, C.-S. Tan, M.H. Huang, Strong facet effects on interfacial charge transfer revealed through the examination of photocatalytic activities of various Cu<sub>2</sub>O-ZnO heterostructures, *Adv. Funct. Mater.* 27 (2017) 1604635.
  - [38] J.-C. Wang, H.-C. Yao, Z.-Y. Fan, L. Zhang, J.-S. Wang, S.Q. Zang, Z.-J. Li, Indirect Z-scheme BiOI/g-C<sub>3</sub>N<sub>4</sub> photocatalysts with enhanced photoreduction CO<sub>2</sub> activity under visible light irradiation, *ACS Appl. Mater. Interfaces* 8 (2016) 3765–3775.
  - [39] Y.-C. Pu, W.-H. Lin, Y.-J. Hsu, Modulation of charge carrier dynamics of Na<sub>2</sub>H<sub>2</sub>·Ti<sub>3</sub>O<sub>7</sub>-Au-Cu<sub>2</sub>O Z-scheme nanoheterostructures through size effect, *Appl. Catal., B* 163 (2015) 343–351.